

Fig. 1. Bathemetric map of study area in the Arctic Ocean. Small rectangles: LSSL and Oden sonobuoy data collected and modeled in P-waves. Thin solid lines: LSSL multichannel reflection lines along these sonobuoy deployments. Green thick lines: Russian OBS lines in the study area. White thick lines: existing refraction lines in the study area. Shaded green area: ocean crust (Chian et al. 2016).

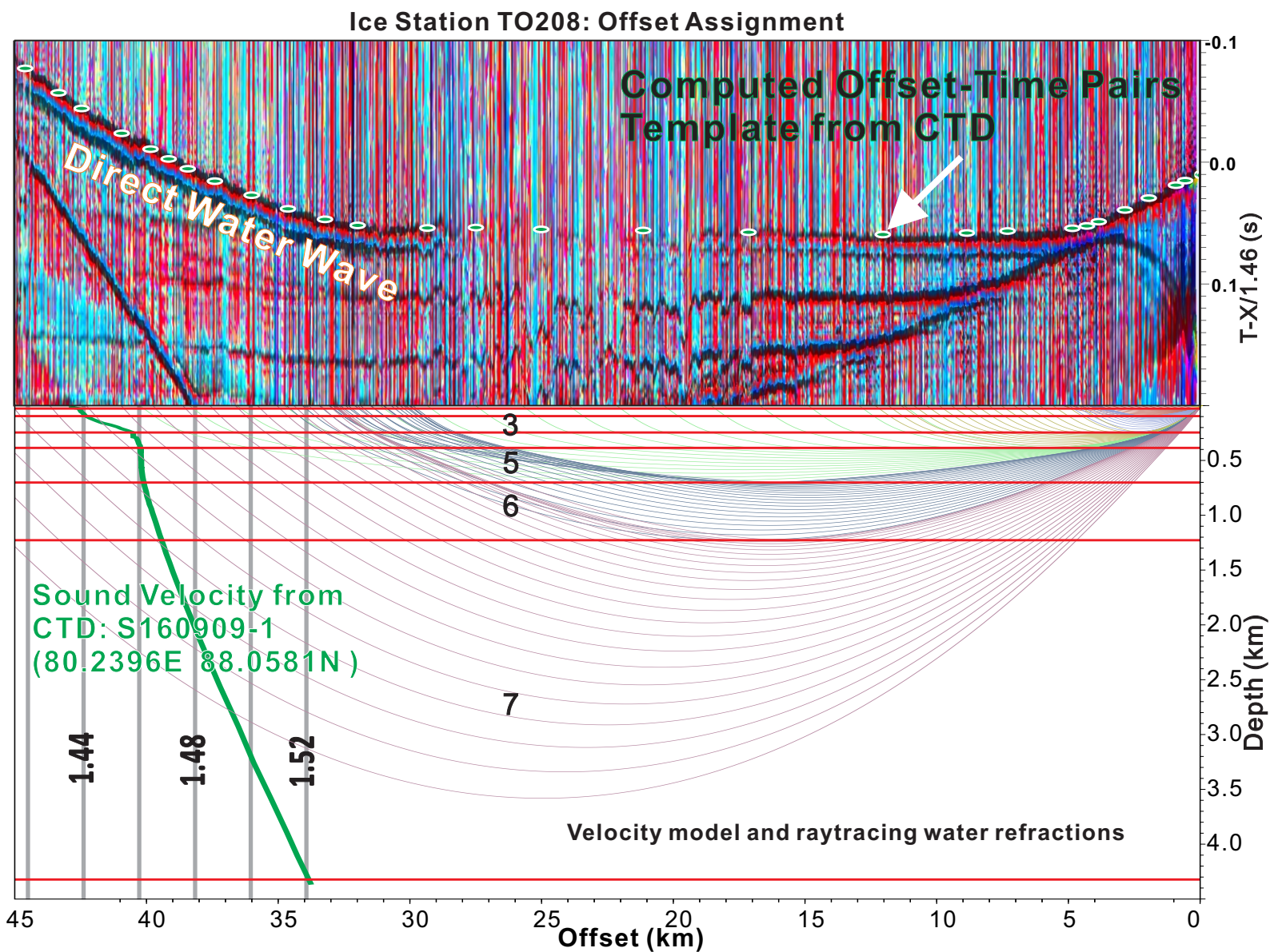


Fig. 2. Top: Example of direct water wave from Ice Station TO208 after offset assignment. Green dots show offset-time computed from model below. Bottom: velocity model of the water layers constructed based on CTD-measured sound velocity profile (thick green line) from a nearby location. See Figure 1 for locations.

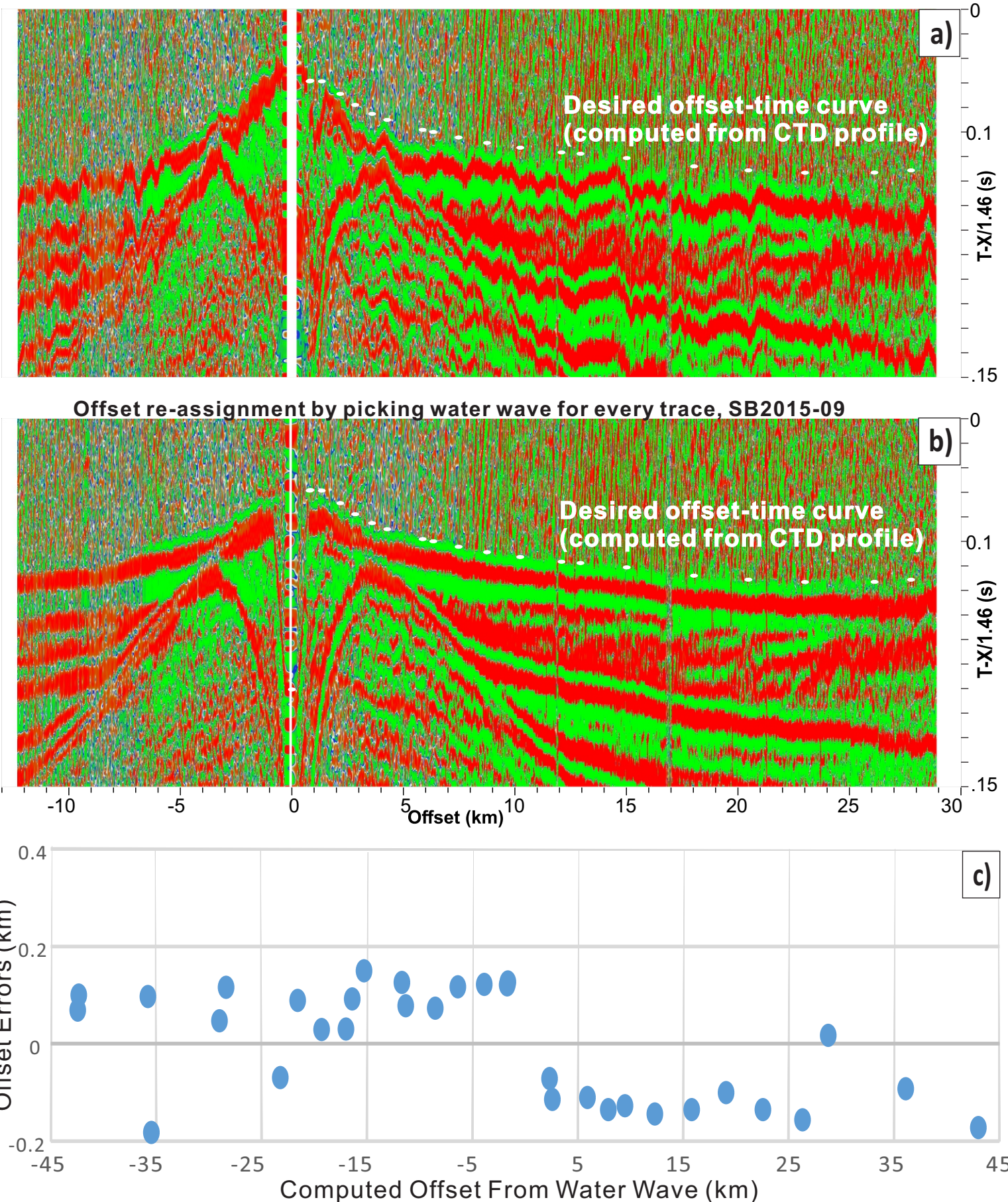
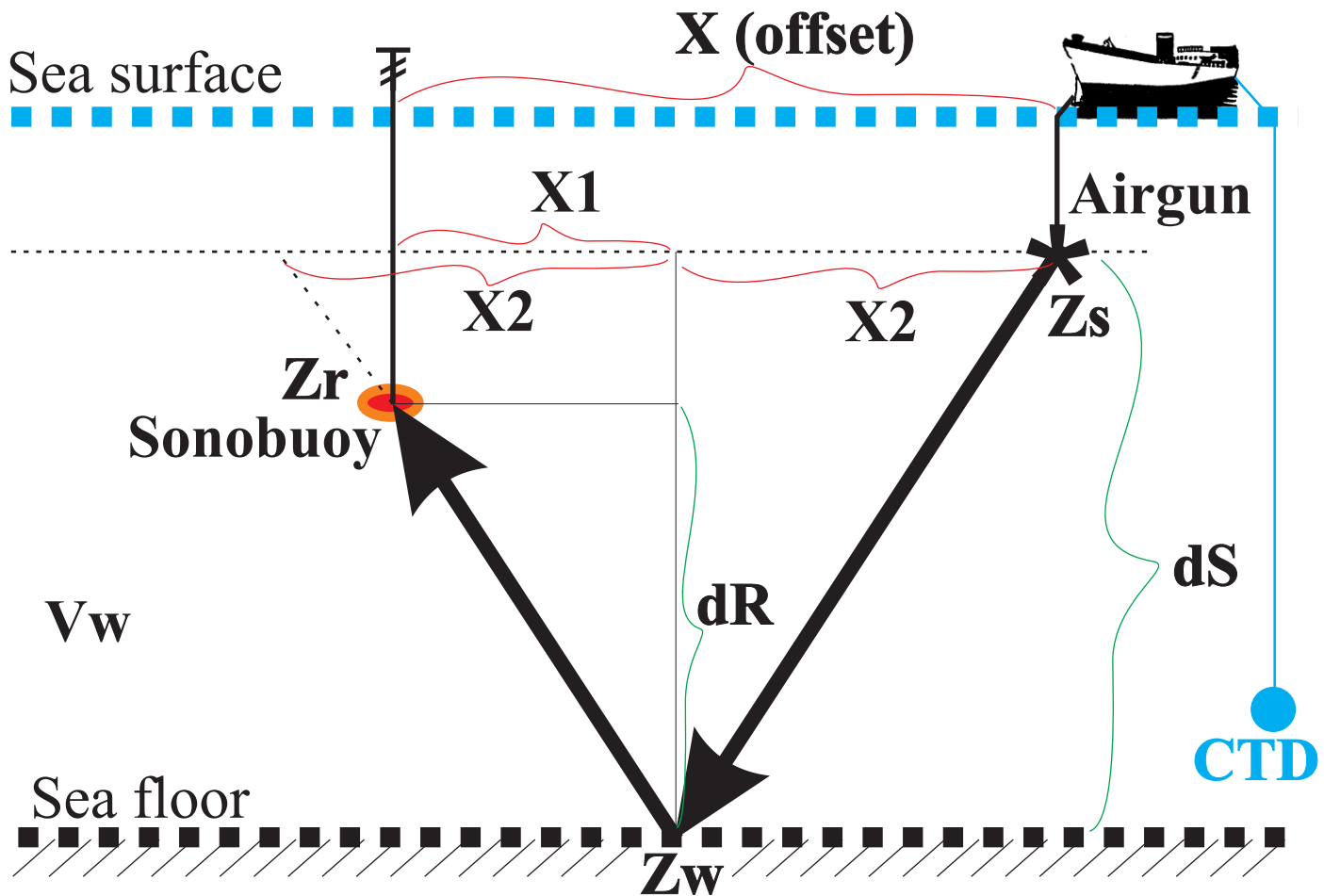


Fig. 3. (a) Offset assignment of sonobuoy 1509 from water wave before picking on every trace, and after water wave picking and offset assigning for every trace (b). Note the jittering of water wave in (a) is smoothed out in (b). (c) Offset errors for ice stations Taurus TL201, TO202, TO405, and TO406. These are difference of offsets from GPS and from direct water wave. It can be seen that all 33 measured points are within an error bound of ± 0.2 km. Note that based on CTD-derived computed curve, an error of 1km in offset would shift the direct water wave by ~ 0.7 sec. See Figure 1 for station locations.



$$X_1 = X_2 * \alpha \quad X_2 = X / (1 + \alpha)$$

where $\alpha = dR / dS$, $dR = Z_w - Z_r$, $dS = Z_w - Z_s$

Fig. 4. Geometry and variables used in determining the time reduction for reduced Normal Move-Out transform. Z_r : receiver (or sonobuoy) depth. Z_s : source (or airgun) depth. CTD: instrument for determining conductivity, temperature, depth and sound velocity.

Sonobuoy LSSL 1103

Deploy: -166.425908W/80.375172N

North →

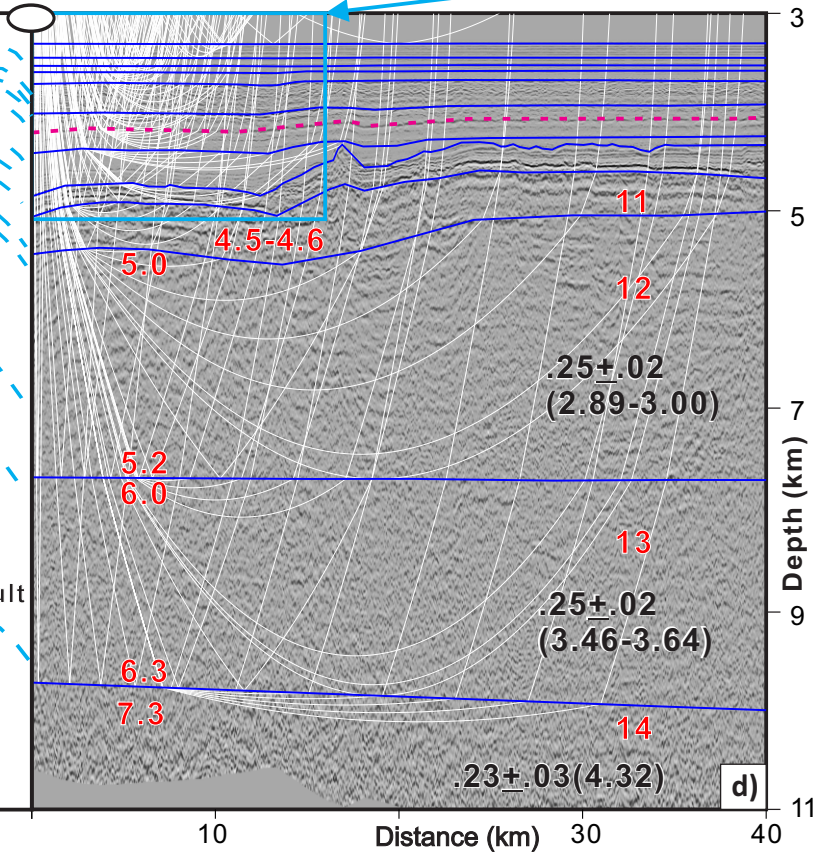
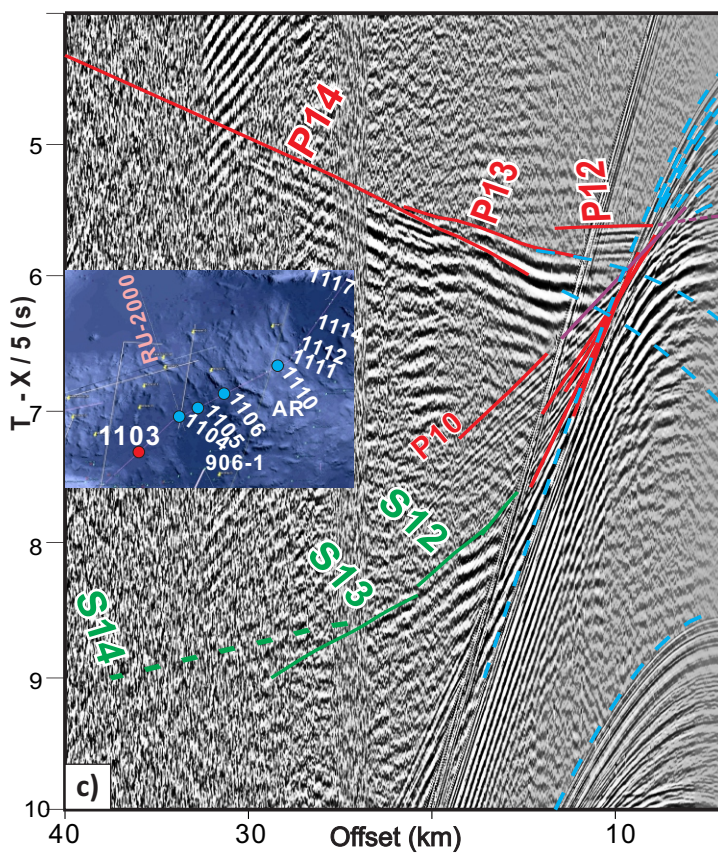
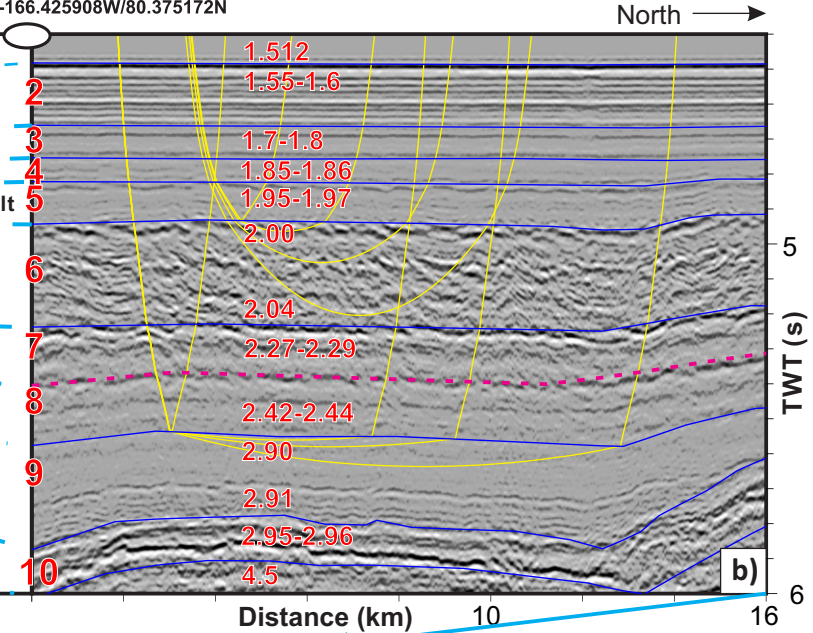
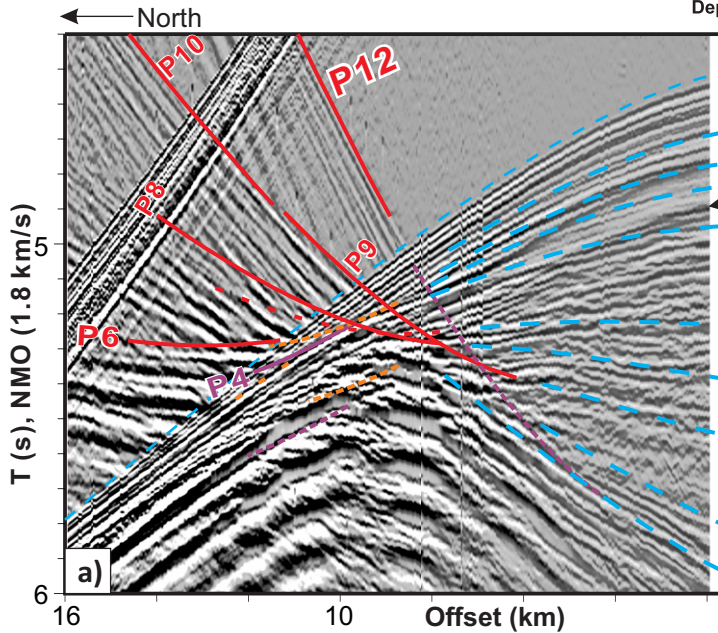


Fig. 5. Two dimensional forward modeling for sonobuoy 1103. a) Sonobuoy record section overlain with computed offset-time plot, RNMO-transformed to match reflection section in b). Sedimentary refractions extend farther to ~20 km offsets but here we only plot up to 16 km offsets for clarity. b) Stacked MCS reflection section overlain by velocity model. Selected refraction raypath (yellow) from layers 6 and 9 are shown. Reverberations of refractions P4 and P5 are marked as dashed lines in a). c) Same sonobuoy record low pass filtered (at 2-12Hz), linearly reduced to show deeper (crustal) refractions. Mult: multiple. d) Crustal model in depth domain, with all P-wave raypaths shown in thin white lines. Black bracketed numbers are S velocities, presided by Poisson's ratios. S12 and S13 in c) are converted S phases refracted from layers 12 and 13, with a modeled Poisson's ratio of .25, converted from P-wave at horizon 8 (dashed red). Modified after Chian and Lebedeva-Ivanova, 2015 except S wave modeling.

Sonobuoy LSSL 1104

Deploy: -168.238017W/81.87536N

North →

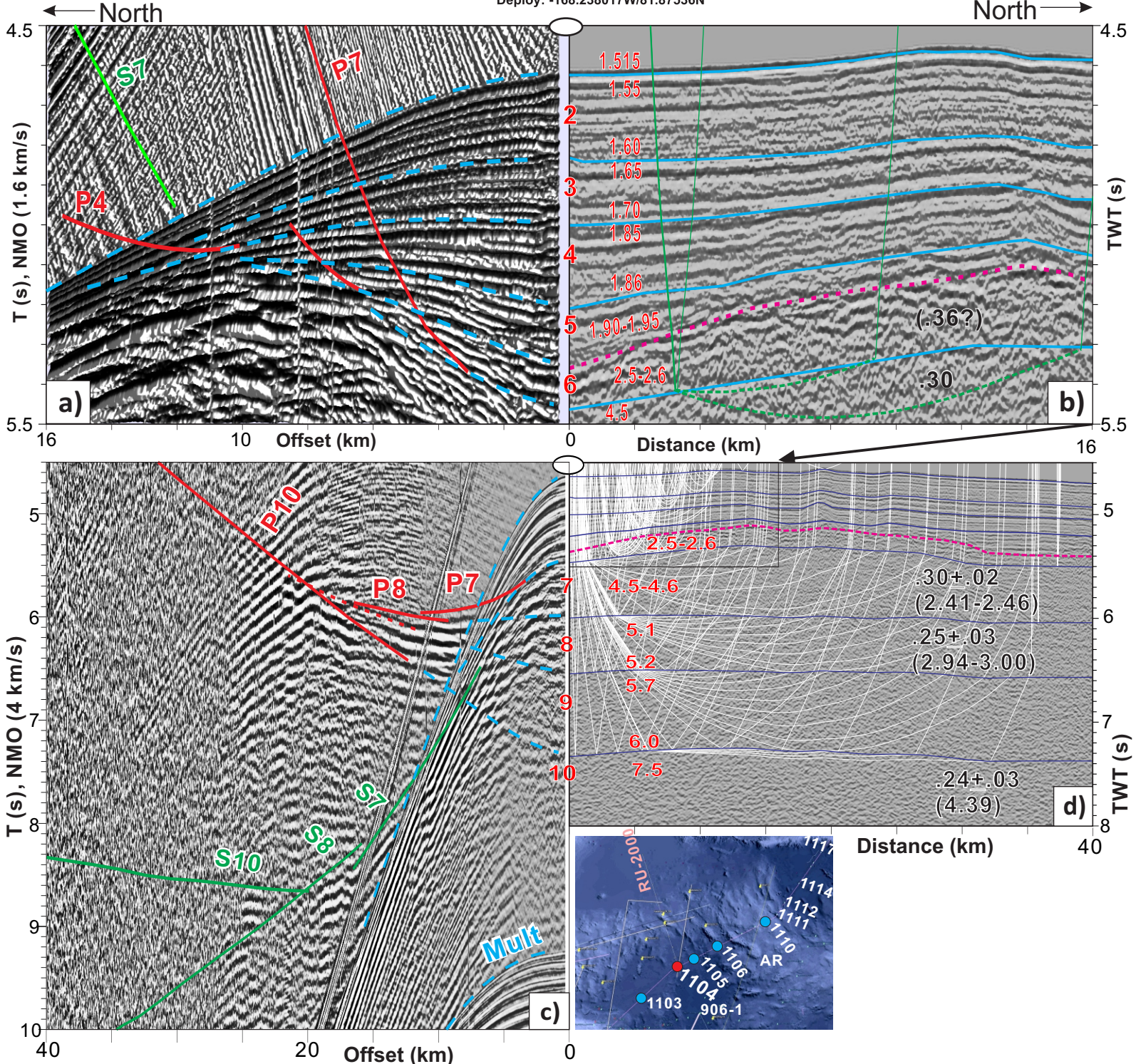


Fig. 6. Modeling of sonobuoy 1104. a) Sonobuoy record section NMO reduced at 1.6 km/s to match coincident reflection profile in b). Green lines show raypaths for converted S-refraction S7 for layer 7. The bracketed Poisson's ratio of 0.36 in layer 6 is assumed as S6 cannot be modeled due to interferences. c) Same sonobuoy section NMO reduced to 4 km/s to show deeper crustal refractions at farther offsets. d) Coincident reflection profile at the same scale as c), overlaid with all P-wave raypaths generating computed XT curves in c). Panels a)-d) modified after Chian and Lebedeva-Ivanova, 2015 except S wave modeling.

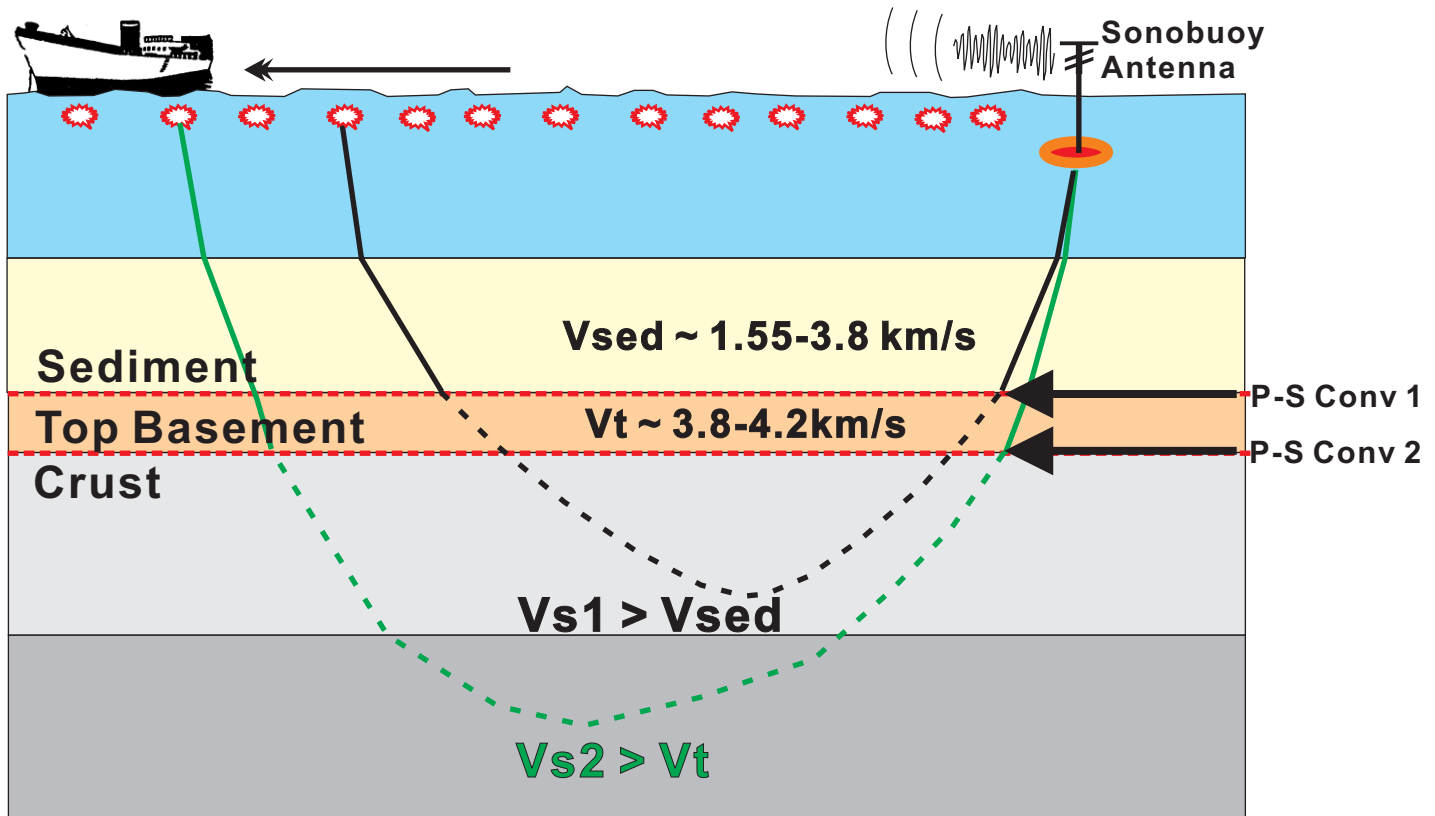


Fig. 7. Cartoon showing dominant P-S conversion interfaces for converted S waves in a marine sonobuoy setting. Solid raypath shows P-waves, while dashed raypath shows S-waves. Condition for “P-S conv 1” follows Eccles et al., 2009. Condition for “P-S Conv 2” applies to deeper crustal layers whose S-velocity (Vs_2) is greater than 4.2 km/s (i.e. V_t ; Fig. 9). S-waves converted at any shallower horizons, if existing, will arrive later and therefore can be obscured and not determinable, unless when their conversions are stronger than basement (e.g. Figure 5).

Sonobuoy LSSL 2009-21-2 (Deploy: 81.9087448N -130.63911438W)

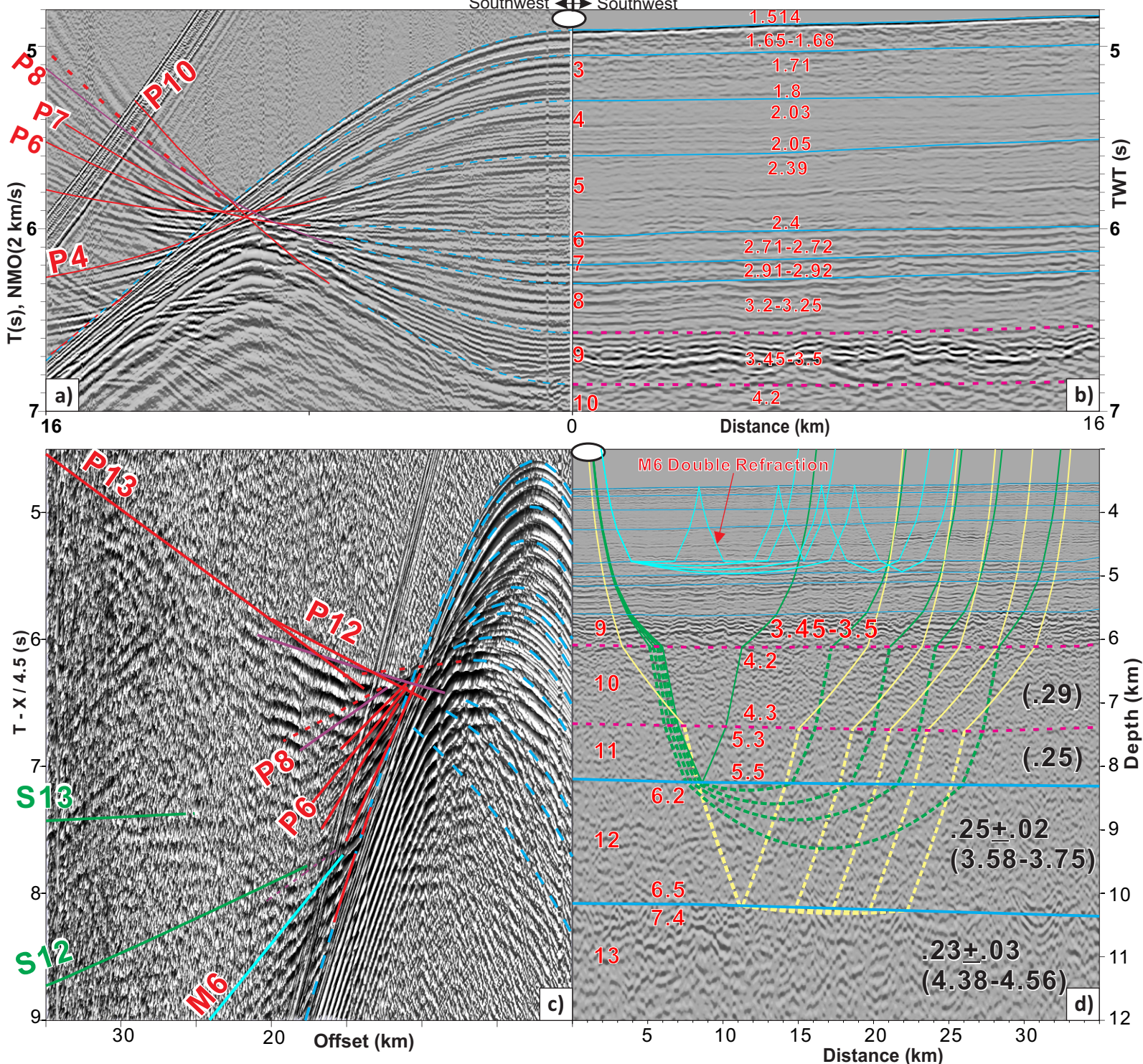


Fig. 8. Modeling sonobuoy 921-2. Raypath in d) shows S-refractions converted at the top of layer 10 (S12) and from top of layer 11 (S13), and for M6 (double refraction of P6 bounced at the seafloor). Modified after Chian and Lebedeva-Ivanova, 2015 except S wave modeling.

Sonobuoy LSSL 912 (Deploy: -146.947057W, 80.765323N)

West →

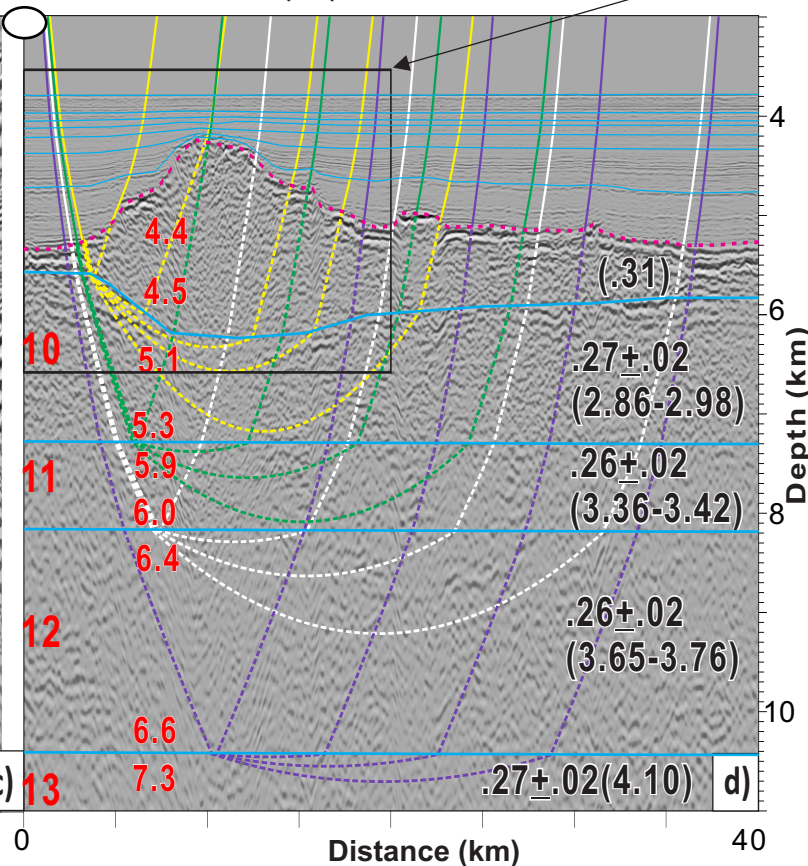
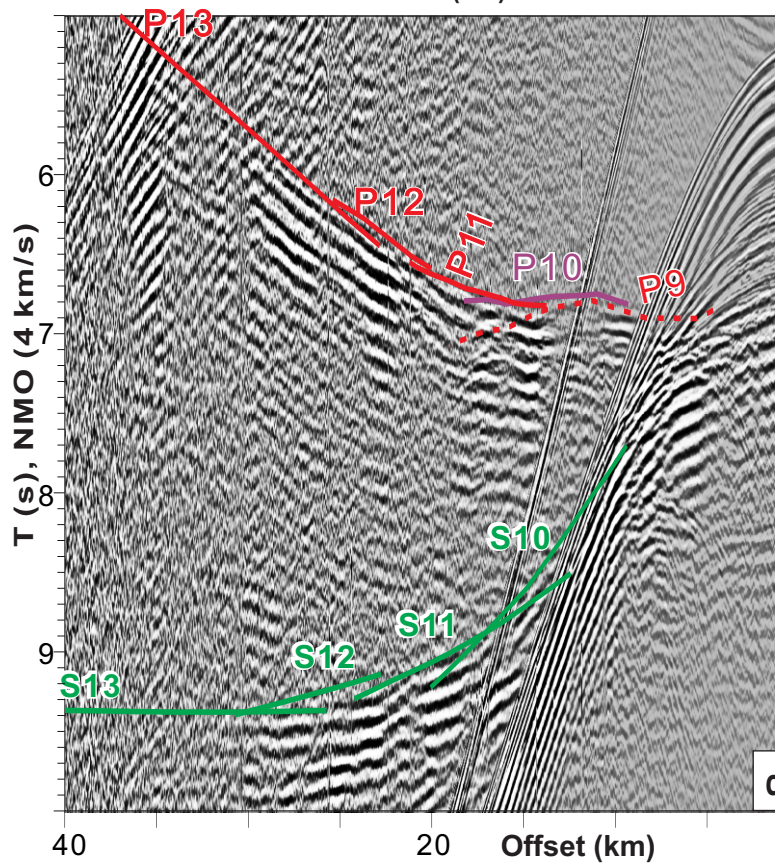
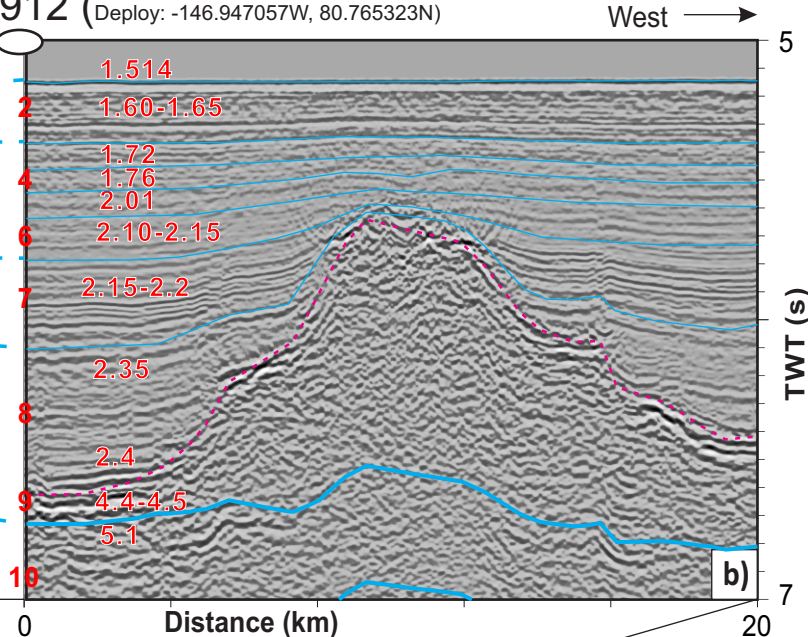
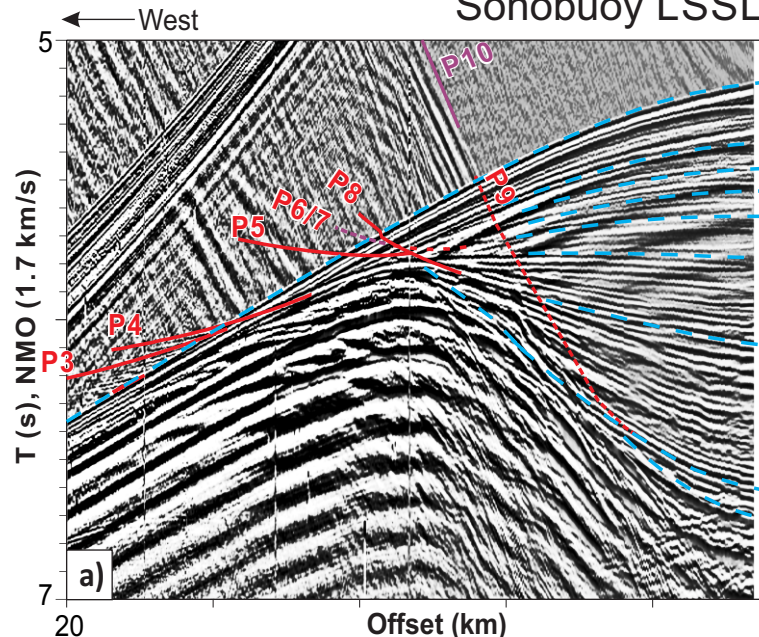


Fig. 9. Modeling of sonobuoy 912. a) Sonobuoy record section RNMO reduced at 1.7 km/s to match coincident reflection profile in b). c) Same sonobuoy section RNMO reduced to 4 km/s to show deeper crustal refractions at farther offsets. d) Coincident reflection profile in the depth domain, overlaid with all S-wave raypaths. Modified after Chian and Lebedeva-Ivanova, 2015 except S wave modeling.

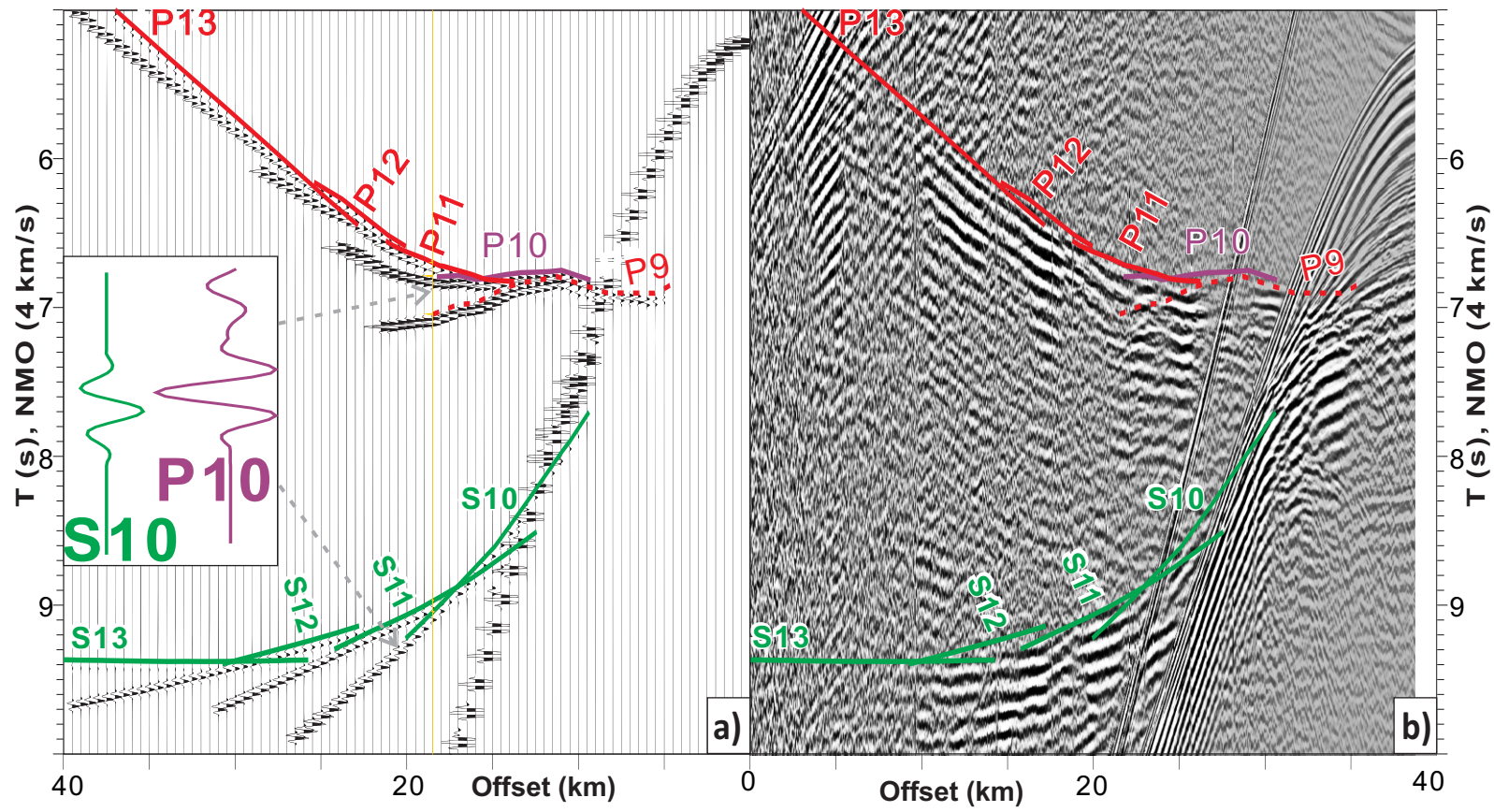


Fig. 10. a) Amplitude modeling of sonobuoy 912 at the same scale as Fig. 9c; inset shows a comparison of computed amplitudes of P10 and S10 arrivals at two arrow locations. Ratio of peak amplitudes of S10 and P10 as in the inset is measured to be 55%. b) Same sonobuoy record section as Fig. 9c for comparison.

Sonobuoy LSSL 1110 (Deploy: -167.01135W, 85.13412N)

South ← → North

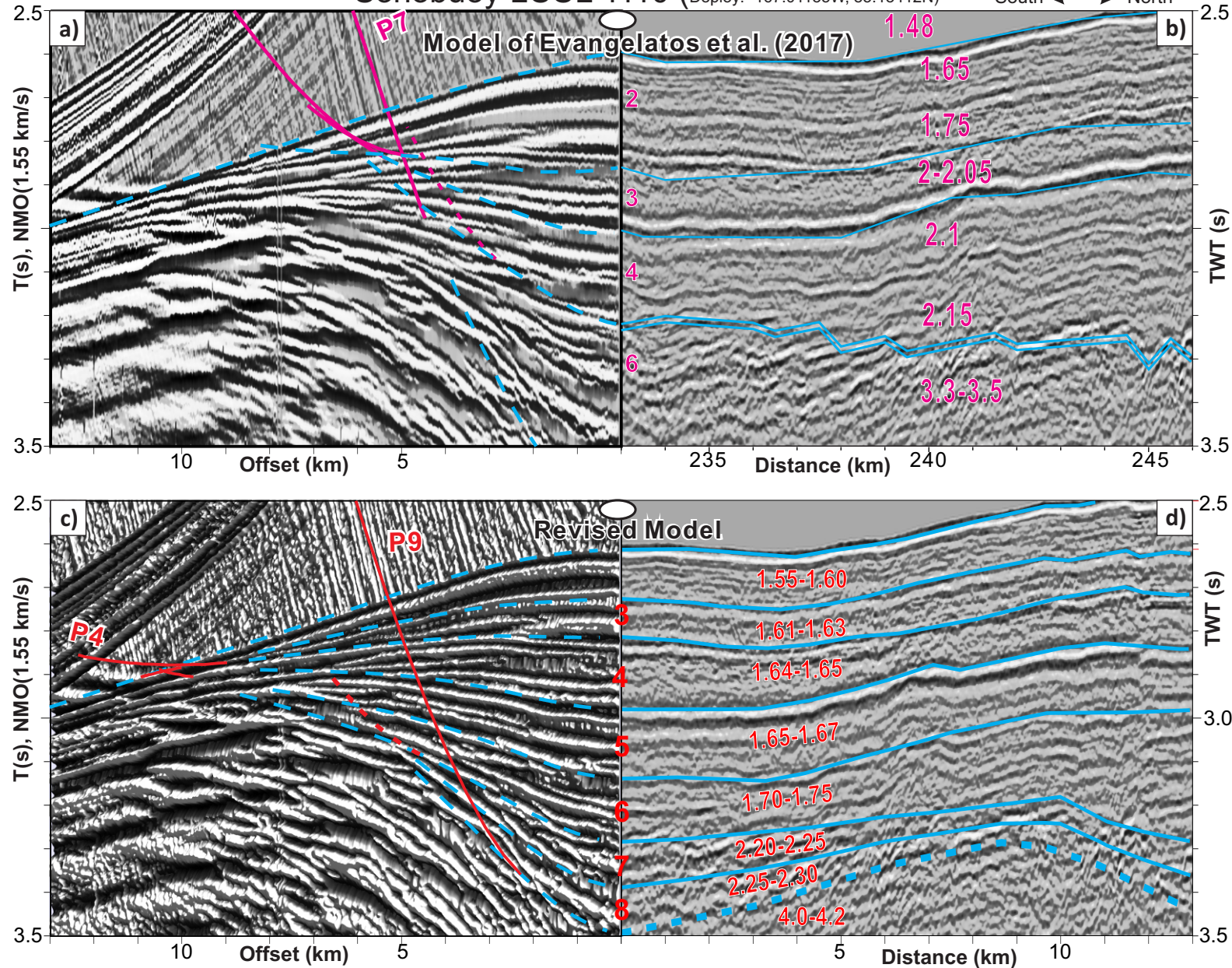


Fig. 11. Re-modeling of sonobuoy record 1110 atop Alpha Ridge. **a)** Area fill display of part of record section, overlain with traveltimes from model in **b)** which was published by Evangelatos et al. (2017). **c)** Same sonobuoy data displayed with 3D shading, overlain with traveltimes from new model in **d)**. It can be seen that all recorded wide-angle reflections and refractions can be modeled visually in detail and more layers can be modeled with the new method presented in this paper. The previously conventional method, however, mostly ignored the wide-angle energy of sonobuoy data during modeling.

Sonobuoy LSSL 1110 (Deploy: -167.01135W, 85.13412N)

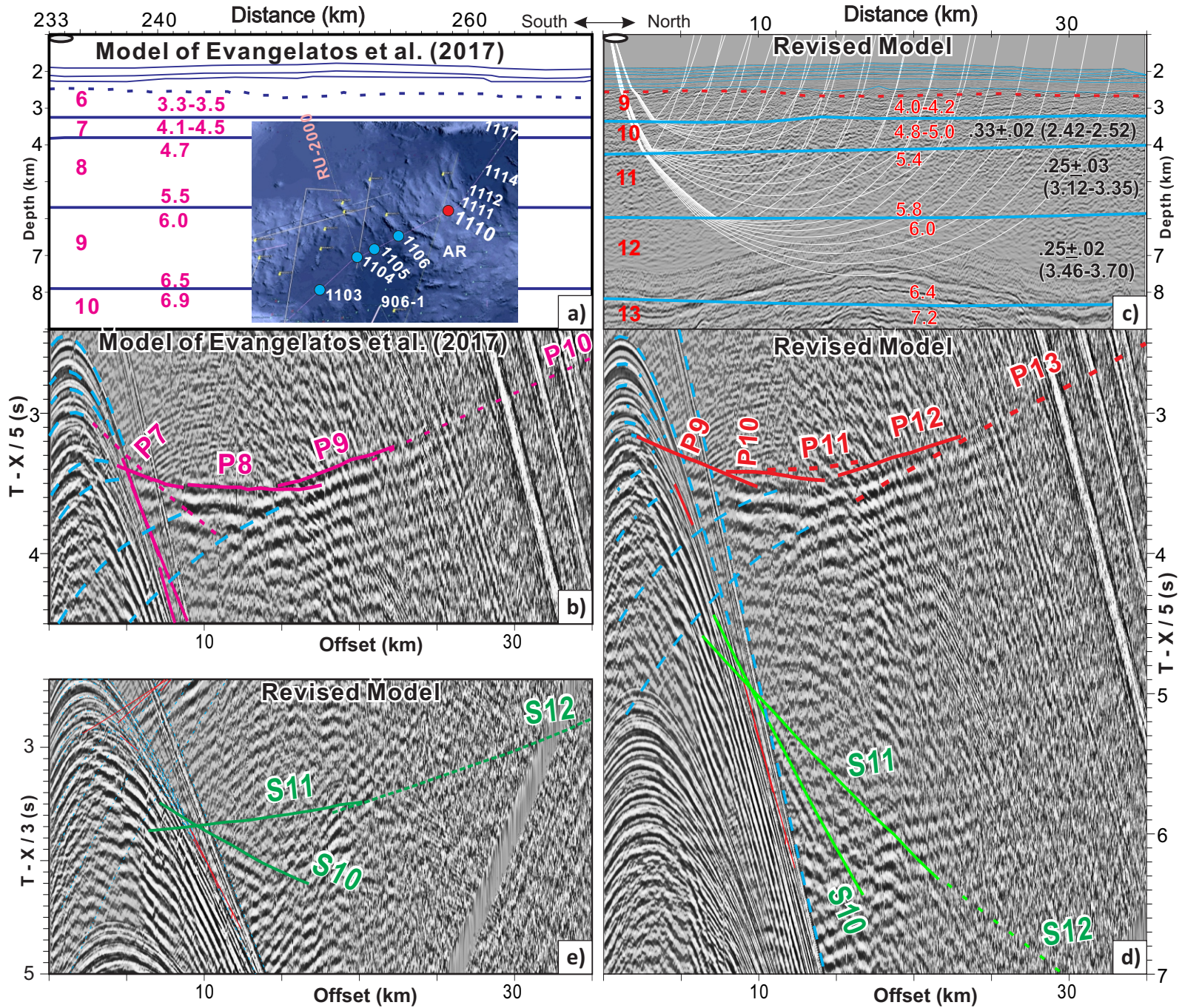


Fig. 12. Re-modeling of sonobuoy record 1110 for sub-basement structure. a) Published crustal model of Evangelatos et al. (2017). b) Computed travel-time curves from this published model. c) Revised crustal model based on the same data, with trace length extended for modeling S phases in d). Selected raypaths shown in c) represent the S-phases from layers 10-12. e) The S phases are more emphasized in e) by using a smaller reducing velocity in display. Note that the refraction P13 from the bottom layer is best modeled by a velocity of 7.2 km/s instead of the slower value of 6.9 km/s by Evangelatos et al. (2017), a change more compatible with other nearby sonobuoys such as 1103 (Figure 5) and 1104 (Figure 6).

Geophysics

1

2 **Application of Reduced Normal Moveout to Model Sonobuoy Refraction Data: A New**
3 **Approach to Integrate Coincident Seismic Reflection Data With Wide Angle Reflections**
4 **and Refractions**

5 Deping Chian¹ and Gordon N. Oakey²

6 ¹Chian Consulting, 6238 Regina Terrace, Halifax, N.S., Canada, B3H 1N5,

7 deping.chian@gmail.com

8 ²Geological Survey of Canada Atlantic, 1 Challenger Dr. Box 1006 Dartmouth, N.S., Canada,
9 B2Y 4A2

10 Key Words:

11 Sonobuoy refraction data

12 Wide-angle reflections

13 Multi-channel seismic reflection data

14 P-wave velocity analysis

15 S-wave seismic conversions

16 Poisson's Ratio

17 Reduced Normal Moveout

Geophysics

18 ABSTRACT

19 Wide-angle reflection and refraction data can be transformed via Reduced Normal-
20 Moveout (RNMO) to closely match every event on coincident multi-channel seismic (MCS)
21 reflection profiles. **These two different datasets are coupled and forward modeled with two-**
22 **dimensional (2D) raytracing to result in velocity structures within sedimentary and crustal layers.**
23 Parametrization of the 2D models are defined with multiple nodes in both horizons and interval
24 velocities using bi-linear interpolations, allowing a complete one-to-one convertible relationship
25 between time and depth domains. Model revisions and perturbations are preferably performed in
26 two-way travel time domain, where velocity and structure relief can be revised for any layer
27 independently without affecting the modeling of other layers. This RNMO methodology has
28 been applied to over 300 sonobuoy records against coincident MCS profiles in the Arctic Ocean
29 where basement relief and crustal structures can be are highly variable and typically very
30 complex. We present examples to demonstrate that the RNMO method can be applied to records
31 with or without refractions, a case difficult to model with traditional modeling approaches.
32 Additionally, we present examples where shear-wave conversions have occurred and
33 demonstrate that the detailed RNMO-derived sedimentary and crustal velocities/structures can be
34 used to determine Poisson's ratios of the crustal layers.

Geophysics

35 INTRODUCTION

36

37 Long-offset refraction seismic methods have been used for decades to acquire acoustic
38 records to determine velocity information of sedimentary and crustal layers beneath the oceans.
39 Such experiments are typically conducted with land recorders, ocean-bottom seismometers, or
40 sonobuoys; the latter are used almost exclusively in the Arctic regions due to perennial sea ice,
41 but seismic recorders are sometimes also deployed on floating sea-ice. Although each of these
42 methods have inherent technical limitations, all record similar acoustic signals: near-offset and
43 wide-angle reflections, long-offset P-wave refractions, multiples, and converted shear-wave
44 refractions (or S-wave refractions).

45 Traditional velocity analysis in reflection seismology typically applies a Normal Move-
46 out (NMO) correction to align and stack hyperbolic reflection energy at small offsets (generally
47 on the order of <5 km or sometimes greater) in order to determine a velocity structure (Dix,
48 1955; Sheriff and Geldart, 1995). However, NMO velocity estimates become more complicated
49 and less reliable in cases of dipping horizons (Yilmaz, 2001), and may fail entirely with
50 multiples and reverberations or with complex structures.

51 For long-offset seismic applications, abundant velocity information is carried to traces at
52 wide angles, which are conventionally determined with forward modelling of first-arrival
53 refractions by two dimensional (2D) raytracing (Zelt and Smith, 1992) or with tomography (e.g.
54 Hobro, 1999). These methods take advantage of the fact that the slope of a refracted phase in the
55 offset-time domain is the reciprocal of the interval velocity of the refraction layer (assuming the
56 structure is flat). Forward modeling of wide-angle reflections, however, is numerically
57 complicated due to their near-hyperbolic nature and offset-varying wavelets, interfered by

Geophysics

58 reverberations and different types of multiples, and is therefore usually not performed as part of
59 the analysis.

60 This paper presents a new method, namely Reduced Normal Move-out (RNMO), which
61 transforms the wide-angle seismic data to produce a display that, at zero offset, correlates
62 directly with the coincident multi-channel seismic (MCS) reflection data. This technique allows
63 an integrated approach to simultaneously model near-offset hyperbolic reflections with long-
64 offset refractions to produce a fine-detailed P-wave velocity model of the sedimentary and
65 crustal layers. The method also permits calculation of various types of multiples to better define
66 long-offset signals.

67 We have applied the RNMO method to over 300 sonobuoys and several ice-deployed
68 seismometers in the Arctic (see dots and small rectangles in Figure 1). In this paper, we present
69 several examples to demonstrate critical components of this methodology, including examples
70 with complex structures. Additionally, each of these examples includes S-wave modeling, which
71 in turn results in estimation of Poisson's ratios for deciphering crustal affinities.

72 DATA ACQUISITION AND MODELING OF WIDE-ANGLE REFRACTION AND 73 NEAR-OFFSET REFLECTION DATA

74 The expendable sonobuoys were deployed from the ship (or sometimes helicopter)
75 during shooting of MCS lines and recorded the same acoustic seismic signals. For the data used
76 in this study, the seismic source was a cluster of 2x500 in³ G-guns plus a 150 in³ G-gun (Mosher,
77 2012). The sonobuoys float in water at a fixed depth (Z_r) with their antenna exposed out of the
78 water for relaying recorded seismic signals via radio transmission to the ship. Typically, the
79 sonobuoys were deployed at 60m water depth, although there were some variations of depth on

Geophysics

80 different cruises (for details see Chian and Lebedeva-Ivanova, 2015). Standard “off-the-shelf”
81 sonobuoys have a 6-hour operational time. With a typical ship’s speed of ~6 km/hr, recorded data
82 rarely exceeded 35-40 km offsets.

83 Raw sonobuoy data were converted to SEGY format for processing. Forward modeling
84 and ray tracing of wide-angle data use the RAYINVR program of Zelt and Smith (1992)
85 combined with commercially licensed software SeisWide (<http://seiswide.hopto.org> ; Chian et
86 al., 2015) to perform all data processing and modeling.

87 When we model sedimentary layers, wide-angle data are filtered at 4-55Hz, while for
88 modeling deeper crustal layers, 2-12Hz are used instead for the filter since higher frequencies
89 deteriorate faster along their paths of traveling. Data de-spiking (e.g. Stanghellini and Bonazzi,
90 2002) or de-noising (e. g, Elboth, 2011) can be useful when necessary. Other processing steps
91 such as deconvolution or F-K filtering were usually not performed, mainly because different
92 kinds of phases may have very different wavelets and slopes, yet our method tries to model all
93 recorded phases.

94 SOURCE-RECIEVER OFFSET ASSIGNMENT

95 Direct water waves are a manifestation of source-receiver distance offsets. To obtain
96 offsets for each recorded trace, we have applied the nearest available acoustic velocity profile
97 measured by CTD (conductivity-depth-density) stations (in Figure 2), preferably in the same
98 cruise, and constructed a one-dimensional velocity model, with typically 7 water layers, each
99 layer assigned a linear vertical velocity gradient that best matches the observed CTD sound

Geophysics

100 velocities. Raytracing was then performed, and the resulting computed refracted time-offset
101 curves are combined to define a template for offset corrections.

102 In practice, the offset assignment is an iterative process. It starts with a preliminary offset
103 assignment based on simple linear interpolation of discrete points on the calculated direct water
104 wave model. When the resulting offset-corrected direct water wave is examined in detail,
105 however, there is still a minor “jitter” from trace to trace (figure 3a). We then picked every trace
106 of the water wave through a semblance-based semi-automatic picking algorithm (Chian and
107 Lebedeva-Ivanova, 2015), and each SEGY trace was assigned an offset based on the offset
108 template already derived above. When these revised data were again displayed, more coherent
109 direct water wave amplitudes sometimes appeared, especially at larger offsets, and we re-picked
110 those portions and again assigned offset corrections. After a few such iterations, and no more
111 changes needed, the offset correction process was completed (Figure 3b). In general, unfiltered
112 data were used at this stage unless the seismic record was very noisy and/or the identification of
113 direct water wave unclear.

114 Estimates show that the offsets obtained from the direct water wave are accurate up to
115 $\pm 0.2\text{km}$ within an offset range of 45km (Figure 3c) for a water depth of 3-4km. This is based on
116 observation of clear direct water wave on GPS-equipped ice stations. Fortunately, direct water
117 waves are always the strongest waves observed compared to all other phases from deeper depth.
118 In the Arctic Ocean, we have found that whenever water waves cannot be convincingly detected,
119 deeper arrivals are not useful as well.

120 A case study of 11 sonobuoy records shows that after deployment, sonobuoys drifted ≤ 2
121 km on average during 6 hours of shooting (Chian and Lebedeva-Ivanova, 2015). Such drifting

Geophysics

122 should have minimal effects on the velocity modeling in most cases because 1) in case of purely
 123 flat layering, sonobuoy drifting has zero effects since raypaths do not change with azimuths; 2)
 124 in other cases, the structures we are targeting are greater than such drifted distances. However,
 125 there were occasionally cases where some sonobuoy's seismic phases cannot be reasonably
 126 modeled, in which case they were smoothed, bulk shifted (assuming sonobuoys shifted in depth),
 127 or discarded.

128 REDUCED NORMAL MOVE-OUT TRANSFORM (RNMO)

129 The purpose of applying the RNMO transform is to tie MCS data with wide-angle events
 130 at zero offset. Figure 4 shows the pertinent geometry. For any given trace at full offset X, the
 131 time can be reduced (or statically corrected) by:

$$132 \quad dT = \frac{\sqrt{X_1^2 + (dR)^2} + \sqrt{X_2^2 + (dS)^2} - (dR + dS)}{V_r} - \frac{Z_r + Z_s}{V_w} \quad (1)$$

133 where $X_1=X_2*\alpha$ and $X_2=X/(1+\alpha)$ are offset contributions from upward and downward rays in the
 134 water column, with $\alpha=dR/dS$, $dR=Z_w-Z_r$, $dS=Z_w-Z_s$, and Z_r the receiver (or sonobuoy) depth, Z_s
 135 the source (or airgun) depth, Z_w the total water depth, V_w average water velocity, and V_r the
 136 desired reduction velocity. If $X = 0$, we have $dT = -(Z_r + Z_s)/V_w$, which indicates that in order to
 137 align the sonobuoy reflections at zero offset with MCS data, we only need to add a one-way
 138 raypath correction for the sonobuoy depth as well as for airgun depth. When X_1 and X_2 are large,
 139 dR and dS become negligible, and we have $dT \approx (X_1 + X_2)/V_r$, which is simply the same as a linear
 140 reduction along a fixed slope defined by V_r . This V_r , the desired reduction velocity, is a useful
 141 variable for displaying wide-angle data; we will demonstrate later that changing V_r from 1.5

Geophysics

142 km/s or 2km/s to 5km/s allows us to change the view focus of wide-angle sedimentary phases to
 143 crustal refractions on the same dataset.

144 After this transform, every reflection event of the sonobuoy data at zero-offset exactly
 145 coincides with MCS reflection data in two-way travel time (TWT) domain. Examples will
 146 follow after we discuss time-depth conversions.

147 TIME-DEPTH CONVERSION AND VICE VERSA

148 Accurate and efficient one-to-one time-depth conversions are crucial in our modeling
 149 scheme. When working in the time domain, any model revisions will involve such conversions at
 150 many points of the model. When a saved depth domain model is re-converted to time domain, its
 151 values must remain the same as the values before saving, otherwise errors will accumulate
 152 during subsequent re-conversions.

153 Time-depth (or vice versa) conversions start from the top layer down, using the formula
 154 for linear velocity gradient (Kaufman 1953) within each layer. Consider a layer with linear
 155 vertical velocity gradient β ; the velocity at the bottom of the layer $v_2 = v_1 (1 + \beta Z)$, where v_1 is
 156 the velocity at the top of the layer, and Z is the layer thickness. To calculate the two-way time t at
 157 any depth z within the layer, we can use:

$$158 \quad t = \frac{2 \ln(1 + \beta z)}{\beta v_1} \quad (2)$$

159 For reverse transform, at any given time t within the layer, its depth z can be calculated by:

$$160 \quad z = \frac{\exp(v_l \beta t / 2) - 1}{\beta} \quad (3)$$

Geophysics

161 At the base of the layer, the time T is related to depth Z by inserting $\beta = (r-1)/Z$ into (2):

162
$$T = 2Z \frac{\ln r}{v_1(r-1)}, \text{ where } r=v_2/v_1 \quad (4)$$

163 When $v_1=v_2$, formula (4) is unstable, and a simple formula for constant velocity should be
 164 used: $Tv_1 = 2Z$ instead. For non-constant velocity layer, (4) is fast to compute for converting
 165 model boundaries (or horizons). To compute for any point within the layer, (2) and (3) can be
 166 used. Sometimes we need to calculate the complete depth array at a small sample rate (e.g. time-
 167 depth conversion for seismic reflection data); in this case it is faster to use a simple constant
 168 velocity formula (i.e. $tv_1=2z$) iteratively instead of the formula (2-4), given the velocity changes
 169 are negligible within the small depth interval (typically 4m as used in this paper).

170 EXAMPLES OF APPLYING RNMO

171 An example (sonobuoy 1103) is shown in Figure 5, where panels a) and b) show details
 172 for the sedimentary section ($V_r=1.8$ km/s) while c) and d) show the complete profile emphasizing
 173 the modeling of the deeper crust ($V_r=5$ km/s). After RNMO transformation, each reflection event
 174 in Figure 5b can be traced into the offset domain, as marked by dashed cyan lines in Figure 5a.
 175 Based on the reflection profile in Figure 5b, a total of 10 sedimentary layers are modeled, each
 176 layer generating a wide-angle reflection up to 10km offsets and refraction up to 16km (or
 177 greater) offsets. While the wide-angle reflections (Figure 5a) from all sedimentary horizons are
 178 well separated at <6km offsets and correlatable with Figure 5b, they quickly become entangled
 179 each other at farther offsets and merged with strong water bottom reflections. Beyond 10 km
 180 offsets, only refractions stand out with their slopes closely match their interval velocities.

Geophysics

181 Velocities in the shallowest layers are easily determined by matching their corresponding
182 wide-angle reflections with a small $V_r = 1.5$ km/s or more (not shown). Adjusting V_r in displaying
183 sometimes also help distinguish multiples from actual horizons (see phase marked as “Mult” in
184 Figure 6a). Sometimes small vertical velocity gradients in the velocity model are required to
185 generate observed refractions (e.g. P9 and P10). Horizon 6 displays a unique “wavy” topology
186 followed by more wavy reflections contributing to well-defined refraction P6. The placement of
187 horizon 7 on the reflection profile is supported by a strong phase near 8-9 km offsets (junction of
188 its wide-angle reflection and refraction, or a triplication point), and the refraction P7 defines the
189 velocity underneath horizon 7. Refraction P8 is recognizable even though it is severely interfered
190 by reverberations of refractions P9 and P10.

191 Crust starts at or below horizon 11 and the reduction velocity (V_r) must be increased to 4-
192 5 km/s (Figure 5c) otherwise deeper refractions are not recognizable. The velocity under horizon
193 11 is assumed to be 4.5-4.6km/s in accordance with regional-scale results, and its resulting
194 refraction P11 is approximately in agreement with record section in Figure 5a. Layer 11 is only
195 ~465m in thickness, underlain by crustal layer 12 producing clear refraction P12 as shown in
196 Figures 4a and 4c. Figure 5c shows the same record section at a V_r of 5km/s (a traditional display
197 of wide-angle data). Phases in this display cannot be directly correlated to near-offset reflection
198 section; the advantage of this traditional display is that the slopes of refractions represent true
199 interval velocities in case of flat layering. For this sonobuoy, the crustal horizons are indeed quite
200 flat, enabling the crustal layers to produce well-defined refractions observed and modeled as
201 P12, P13, and P14. It is noteworthy that at far offsets, refracted rays commonly dive in their
202 medium without diffractions or energy splitting, which is unlike reflections that have only partial

Geophysics

203 energy reflected back to the recorders. Therefore at large offsets, one can see refracted phases
204 even despite very limited recorded seismic energy from the airgun sources.

205 While the geometries of refractions are a direct manifestation of interval velocities in
206 their corresponding layers, sometimes they do not show up in record sections, and the RNMO
207 transform allows us to use the wide-angle reflections to constrain the interval velocities. Figure 6
208 show such a case with modeling for sonobuoy 1104. Only refraction P4 is observed modeled by
209 a small velocity gradient (1.85-1.86km/s), while velocities of all other sedimentary layers are
210 determined from forward modeling wide-angle reflections in the sonobuoy record section.
211 Experience indicates that when no refracted phases exist, it is convenient to represent each layer
212 with a larger linear vertical velocity gradient (at a difference of 0.05-0.15 km/s between top and
213 bottom of the layers).

214 Another advantage of the RNMO transform is the convenience of model revisions while
215 working in the time domain: velocity updates can be done in any layer without affecting deeper
216 horizons. If working in the depth domain, however, when a layer's velocity changed, the depths
217 of all horizons underneath will need to be revised as the reflection times are fixed, a process
218 automatically taken care of when working in the time domain.

219 ERROR ESTIMATES

220 To estimate error in the velocities of sedimentary layers, the velocity values in the time
221 domain can be perturbed and the resulting computed travel-time curves assessed. We choose to
222 do this in the time domain because the time of each horizon will not change with the
223 perturbation, regardless of the horizon depth changes (δZ). A list of possible velocity error (δV)

Geophysics

224 for each layer is then compiled (see Table 1). Two extreme velocity models in the time domain
 225 can be derived, each representing the maximum and minimum possible velocities in each layer.
 226 When these extreme models are converted to the depth domain, the depth difference of each
 227 horizon, δZ are added to Table 1. As can be seen from Table 1, the resolution associated with the
 228 error in velocity is less than 4%. The depth resolution of basement is 0.6% for both sonobuoys,
 229 which accounts for +30m for both sonobuoys 1103 (Figure 5) and 1104 (Figure 6). **Note that**
 230 **anisotropy is not taken into account here, which will be discussed further in the following section**
 231 **as well.**

Layer	δV (km/s)	$\delta V/V$ (%)	$\delta Z/Z$ (%)	(V1-V2) (km/s)	δZ (km)	Ztop(km)	Ttop(s)
2	0.05	3.175	0.074	(1.525-1.625)	.005	3.421	4.632
3	0.05	2.99	0.196	(1.623-1.722)	.014	3.584	4.839
4	0.02	1.078	0.262	(1.835-1.875)	.02	3.714	4.994
5	0.05	2.597	0.317	(1.875-1.975)	.026	3.883	5.176
6	0.03	1.176	0.371	(2.520-2.580)	.03	4.009	5.308
7	0.1	2.198	0.62	(4.450-4.650)	.059	4.171	5.435

232 *Table 1. Error analysis of layer velocities and depths for sonobuoy 1104 (Figure 6). $\delta V/V$ and $\delta Z/Z$ are*
 233 *maximum deviation in percentage from average velocity and depth for each layer. V1-V2 are range of*
 234 *average velocity for the two perturbed models. Ztop and Ttop are depth and time of top horizon of each*
 235 *layer for the un-perturbed model. Bold lines indicate basement layer, below which the error analysis*
 236 *method does not apply due to lack of control from reflection profile.*

MULTIPLES AND CONVERTED WAVES

238 Sonobuoy records include various kinds of seismic energy, many of which can be
 239 coherently identified. In addition to the first arrivals, the 2D forward model method of Zelt et al.
 240 (1992) that we adopted allows modeling of multiples, and sometimes converted S waves that are
 241 refracted from crustal layers.

242 Figure 7 illustrates the scenarios of S wave double conversions that enable observation
 243 and modeling of S refractions in a marine environment. Since the water layer prohibits travelling

Geophysics

244 of S-waves, S-refractions must be double converted at some major boundaries (or horizons), as
 245 marked by “P-S Conv 1” and “P-S Conv 2”. The “P-S Conv 1” is at the basement surface and
 246 was described by Eccles et al. (2009), who argued that converted S refractions in marine
 247 experiments cannot be observed if along the ray paths there is a velocity $V_{\text{sed}} \geq V_{s1}$, where V_{s1}
 248 is the S velocity in the refracted layer. The basement surface is usually the best candidate for the
 249 P-S double conversions, and any S waves converted at shallower horizons will arrive later and
 250 obscured by reverberations or other phases. S phases converted from the seafloor were
 251 occasionally observed when the sedimentary layer is thin, but they do not appear to co-exist with
 252 basement-converted S phases.

253 P-S double conversion is well exemplified in sonobuoy 1103 (Figure 5), where the S
 254 waves (S12 and S13, and maybe S14) can be identified by their lower frequency than
 255 sedimentary phases (e.g. P10), and lack of corresponding parallel P-wave refractions. These
 256 phases are best modeled as converted at horizon 8 (dashed green), travelling as S waves
 257 downward and refracted within their corresponding layers, and converted back to P-waves at the
 258 same horizon 8. A Poisson’s ratio of 0.25 is used during the modeling of S12 and S13. Similarly,
 259 sonobuoy 1104 (Figure 6) has S7, S8, and S10 phases modeled as refracted S refraction from
 260 crustal layers of Poisson’s ratios of 0.30, 0.25, and 0.24, respectively. The converting interface is
 261 usually selected to be a strong reflective horizon, which is mostly at or near the basement
 262 surface. For generating S12 with a Vs of 2.89 km/s in Figure 5, for example, the deepest
 263 conversion can be horizon 9 ($V_p=2.42$ km/s) or 8, with the latter selected since the former would
 264 produce an S12 too early. Since it is common that converted S refractions do not appear for every
 265 layer, for those that do not have seismic controls, we rely on trial and error method to make a
 266 best guess on Vs for all S-trespassed layers (see bracketed Poisson’s values in Figure 6d), which

Geophysics

simply shifts computed travel-time curves up and down in time. The error bars of the Poisson's ratios are estimated by perturbing the values until the fit to the phase slope cannot be accepted, commonly with ± 0.01 for excellent P and S phases, and ± 0.03 for poor P and/or S phases. The Poisson's ratios thus obtained are compatible with nearby S-wave observations from the ocean bottom seismometers (OBS) observations on Arctic-2012 by Kashubin et al. (2016).

Another type of P-S double conversion has been observed in the Arctic study areas and modeled at "P-S Conv 2" in Figure 7, where the top part of the basement has a P-velocity (Vt) of 3.8 to 4.2 km/s which is smaller than the S-velocity (Vs2) in the deep crust: $Vs2 > Vt$. An example is shown in Figure 8, where S13 is modeled as an S-refraction from a layer with $Vs \geq 4.38$ km/s, with its rays (Figure 8d) doubly converted at the base of layer 10. Such S13 phase is usually regarded as noise without detailed investigation as here. Meanwhile, S12 is modeled as S-refraction doubly converted at the top of layer 10 (or P-S Conv 1).

In identifying S waves, one must be careful not to confuse them with "double refractions", which we refer to as sedimentary refractions bounced downward and get refracted again at the same layer (see M6 and its raypath in Figure 8d). We have found that double refractions are observed more frequently than S waves in the Arctic, and can be distinguished from S waves by their higher frequencies and different (albeit similar) slopes.

Converted S refractions are meaningful only when their corresponding P refractions are observed and convincingly modeled. To estimate the possible errors of the resulting Poisson's ratios, we first obtain the error bounds of Vp (e.g. 0.2, 0.3, and 0.3 km/s for P7, P8, and P10 in Figure 6), and perturb the Poisson's ratios at two error bounds of Vp, until a mis-match of S

Geophysics

288 refractions is reached. This perturbation results in $.30 \pm .02$, $.25 \pm .03$, and $.24 \pm .03$ for layers 7, 8
289 and 10 as shown in Figure 6d.

290 Anisotropy adds another complication to the study; it implies smaller sound velocities
291 vertically than horizontally due to compaction (e.g. Bachman, 1983). But without enough
292 seismic data coverage, anisotropy is just an uncontrolled variable that can change model values.
293 Under the resolution of our experiments, we have found that it is simpler and easier ignore
294 anisotropy, and the resulting velocity models can satisfy the matching of all refraction, wide-
295 angle reflection, and MCS reflection data.

296 APPLICATION TO COMPLEX STRUCTURES

297 Our method presented above has been applied to hundreds of sonobuoy deployments in
298 the Arctic (Figure 1), where it is found to work even for complex structures. As an example,
299 Figure 9 shows the modeling of sonobuoy 912, where the RNMO-transformed section closely
300 matches the coincident reflection profile that is severely intruded by volcanics from below. Many
301 short segmented refractions can be identified and modeled (Figure 9a) during the modeling
302 process. Refractions from basement surface (P9) are seldom observed due to their extreme
303 complexities in structures and rock properties. But an assumed velocity of 4.4-4.5km/s for this
304 layer produces a refraction curve P9 that matches the general appearance in Figure 9a although
305 the phase is intersected at wide angles by various kinds of reflections and reverberations.

306 To examine deeper phases, one must increase the reducing velocity V_r of RNMO
307 transform to typically ≥ 4 km/s (Figure 9c), otherwise it is almost impossible to work with the
308 deeper data properly. For this sonobuoy, we can identify and model 5 crustal refractions (P9-
309 P13), and their corresponding velocities are indicated in Figure 9d, although less number of

Geophysics

310 layers may also work depending on the choices of different authors. Converted S crustal
311 refractions can be identified, modeled, and correlated to their own P refractions. As a test, we
312 generated a synthetic amplitude profile using the velocity model in Figure 9d, and the results are
313 compared to the sonobuoy record using nearly the same display parameters as shown in Figures
314 10a and 10b. The amplitude ratio of S10 versus P10 at the arrow locations is about 55% (see
315 inset of Figure 10a). S12 is strongly interfered by other phases (i.e. S11 and S13) but the many
316 reverberations of S12 help delineate its slope. The resulting Poisson's ratios (0.26-0.27) are
317 greater than other surrounding sonobuoys (e.g. 1103 and 1104), which can be explained by
318 influence of volcanic intrusions that resulted in mixing of sediments, water and cracking with
319 extruded volcanic materials, a process that slows down the S-velocities. With the presence of
320 complex structures like in Figure 9, it is not surprising to note that separate models (instead of
321 one unified model) are required represent long seismic lines when sonobuoys are spaced farther
322 than structure sizes. In places where sonobuoys only record data at large offsets, one can resort to
323 a regionally-compiled exponential model of inverse velocity-depth for the sedimentary velocities
324 (Shimeld et al., 2016), and still continue to model deeper arrivals.

325 COMPARISON TO A NEARBY PUBLISHED SONOBUOY RESULT

326 We have found that velocity models obtained via traditional modeling methods on wide-
327 angle seismic data are frequently not fitting when the same wide-angle data are RNMO-
328 transformed and checked against coincident MCS data. Figure 11 shows such an example with
329 sonobuoy 1110 on the Alpha Ridge (see Figure 1 for location), where Evangelatos et al. (2017)
330 obtained a unified velocity model along a 650 km line controlled by 9 sonobuoy wide-angle
331 profiles. When the sedimentary reflectors of the sonobuoy wide-angle profile is displayed via
332 RNMO transformation, they do not fit the computed travel time curves except the seafloor

Geophysics

333 reflection (Figure 11a). When displayed side by side with the coincident MCS data in Figure 11b,
334 the horizon depths are also loosely connected to major reflectors. There is a clear refraction that
335 was not included in the model, although this may be explained by due to existence of too much
336 horizontal topography in a single model along a long line and not all geometries can be included.

337 In Figures 11c and 11d we try to re-do the modeling using RNMO transform. The
338 sonobuoy data in Figure 11c are the same data as in Figure 11a but displayed in 3D shaded relief
339 for easier presentation of different phases. When the MCS data are displayed together, it is
340 straightforward to derive a model of 8 layers that match all reflectors in the MCS data on the
341 right, and at same time can be ray traced to produce correct travel-time curves for the observed
342 events (including refraction P4) in the sonobuoy wide-angle data on the left. Some clear
343 reflections in the Sonobuoy data (e.g. inside layers 4 and 5) do not have any correspondents in
344 the MCS data, and can be attributed to reverberations given the sonobuoy data are not de-
345 convolved.

346 In Figure 12 we compare the deeper crustal models for this sonobuoy. In the old model in
347 Figure 12a, the 3.3-3.5km/s velocity (layer 6) does not exist in the data, and in our model we
348 replaced it with 4.0-4.2km/s (P9). P10 and P12 are well observed and modeled in Figure 12d, in
349 between whom we inserted an extra layer 11, whose refraction P11 is not clear but supported by
350 reverberations at greater travel time. The introduction of layer 11 also allows modeling its S-
351 refraction, S11 as can be seen in panels d and e. The layer 13 has a higher velocity of 7.2 km/s in
352 our model (as opposed to 6.9 km/s in the old model) and it appears to produce a better overall fit,
353 more compatible with re-modeling of other surrounding sonobuoys (not shown).

Geophysics

354 CONCLUSION

355 Traditional near-offset reflection (MCS) profiles at sea can be augmented with wide-
356 angle reflection and refraction recordings from external stations such as sonobuoys (or ice
357 stations, ocean bottom seismometers et al.). These wide-angle data carry abundant velocity
358 information for nearly every reflection event at up to 40 km offset. Applying the new RNMO
359 transform to the wide-angle data, all MCS reflection events can be visually correlated with wide-
360 angle reflection and refractions when plotted at the same scale. 2D raytracing and modeling of
361 these data reveal the details of the velocity variations, which are parameterized by bi-linear
362 interpolations of selected nodes in time or depth domains. It is more convenient to do model
363 revisions in the time domain where the time is based on MCS events. Such a modeling scheme
364 allows one-to-one accurate conversion between time and depth domains using analytical formula
365 (3-4), or via a simple iterative algorithm when all trace samples are to be converted. This method
366 can be applied to complex structures and long profiles, as exemplified along a transect across the
367 southern Alpha Ridge in the Arctic, where sedimentary refractions are observed in the south
368 (Figure 5) but only wide-angle reflections can be identified in the north (Figure 6). In addition,
369 deeper crustal structures can be revealed similarly by modeling refractions at large offsets, with
370 modeling S refractions (and Poisson's ratios as a result) when they are observed.

371 ACKNOWLEDGMENTS

372 The officers and crews of the CCGS Louis S. St Laurent and the USCGC Healy are
373 thanked for their tireless efforts in the ice choked waters of the Arctic Ocean in support of the
374 scientific program. The experience, skill and unflagging support of the seagoing technical team
375 lead by Borden Chapman were the key to the success of the program. Funding for this work was

Geophysics

376 provided through the Geological Survey of Canada as part of the Canada's Extended Continental
377 Slope (ECS) Program. This is ESS contribution no. XXXXXXXX.

378 The manuscript was internally reviewed by R. Courtney and J. Shimeld. In addition, this
379 manuscript was improved through critical reviews of XXX.

380

381 REFERENCES

382 Bachman, R. T., 1983, Elastic anisotropy in marine sedimentary rocks: Journal of
383 Geophysical Research, **88**, 539–545.

384 Chian, D., H.R. Jackson, D.R. Hutchinson, J.W. Shimeld, G.N. Oakey, N. Lebedeva-
385 Ivanova, and Q. Li, 2016, Distribution of crustal types in Canada Basin, Arctic Ocean:
386 Tectonophysics, **691**, 65-84.

387 Chian, D. and Lebedeva-Ivanova, N., 2015. Atlas of Sonobuoy Velocity Analyses in
388 Canada Basin; Geological Survey of Canada, Open File 7661, 55 p., 1 zip file.
389 doi:10.4095/295857.

390 Dix, C.H., 1955, Seismic velocities from surface measurements, Geophysics, **20**, 68-86.

391 Eccles, J.D., R.S. White, and P.A.F. Christie, 2009. Identification and inversion of
392 converted shear waves: case studies from the European North Atlantic continental margins,
393 Geophys. J. Int., **179**, 381-400.

Geophysics

- 394 Elboth, T., I.V. Presterud, and D. Hermansen, 2010, Time-frequency seismic de-noising:
395 Geophysical Propecting, **58**, 441-453.
- 396 Funck, T., H.R. Jackson, and J. Shimeld, 2011, The crustal structure of the Alpha Ridge at
397 the transition to the Canadian Polar Margin: Results from a seismic refraction experiment:
398 Journal of Geophysical Research, **116**, B12101.
- 399 Hobro, J. W., 1999, Three-dimensional tomographic inversion of combined reflection and
400 refraction seismic travel-time data, Ph.D. dissertation, University of Cambridge.
- 401 Kashubin, S., O. Petrov, I. M. Artemeva, N. A. Krupnova, 2016, Deep structure of crust
402 and the upper mantle of the Mendeleev Rise on the Arktic-2012 DSS profile: УДК 65, 16-35.
- 403 Kaufman, H., 1953, Velocity functions in seismic prospecting: Geophysics, **18**, 289-297.
- 404 Lebedeva-Ivanova, N., 2010, Geophysical studies bearing on the origin of the Arctic
405 Basin: Ph.D. thesis, Uppsala University.
- 406 Mosher, D.C. (ed), 2012, 2011 Canadian High Arctic Seismic Expedition: CCGS Louis S.
407 St-Laurent expedition report, Geological Survey of Canada, Open File 7053.
- 408 Sheriff, R. E., and L.P. Geldart, 1995, Exploration Seismology (2nd ed.), Cambridge
409 University Press.
- 410 Shimeld J., Q. Li, D. Chian, N. Lebedeva-Ivanova, R. Jackson, D. Mosher, and D.
411 Hutchinson, 2016, Seismic velocities within the sedimentary succession of the Canada Basin and

Geophysics

412 southern Alpha-Mendeleev Ridge, Arctic Ocean: evidence for accelerated porosity reduction?:

413 Geophysical Journal International, **204**, 1-20.

414 Stanghellini G., and C. Bonazzi, 2002, Local-trace zeroing and spike zeroing: two short

415 automated noise-rejection routines to remove noise and spikes on seismic traces: Geophysics **67**,

416 188-196.

417 Yilmaz, Öz, 2001, Seismic data analysis: Society of Exploration Geophysicists.

418 Zelt, C.A., and R.B. Smith, 1992, Seismic travel time inversion for 2D crustal structure:

419 Geophysical Journal International, **10**, 16-34.

Geophysics

420 LIST OF FIGURES

421 Figure 1. Bathemetric map of study area in ther Arctic Ocean. Small rectangles: LSSL
422 and Oden sonobuoy data collected and modeled in P-waves. Thin solid lines: LSSL multichannel
423 reflection lines along these sonobuoy deployments. Green thick lines: Russian OBS lines in the
424 study area. White thick lines: existing refraction lines in the study area. Shaded line green area:
425 ocean crust (Chian et al. 2016).

426 Figure 2. Top: Example of direct water wave from Ice Station TO208 after offset
427 assignment. Green dots show offset-time computed from model below. Bottom: velocity model
428 of the water layers constructed based on CTD-measured sound velocity profile (thick green line)
429 from a nearby location. See Figure 1 for locations.

430 Figure 3. (a) Offset assignment of sonobuoy 1509 from water wave before picking on
431 every trace, and after water wave picking and offset assigning for every trace (b). Note the
432 jittering of water wave in (a) is smoothed out in (b). (c) Offset errors for ice stations Taurus
433 TL201, TO202, TO405, and TO406. These are difference of offsets from GPS and from direct
434 water wave. It can be seen that all 33 measured points are within an error bound of +0.2km. Note
435 that based on CTD-derived computed curve, an error of 1km in offset would shift the direct
436 water wave by ~0.7sec. See Figure 1 for station locations.

437 Figure 4. Geometry and variables used in determining the time reduction for Reduced
438 Normal Move-Out transform. Zr: receiver (or sonobuoy) depth. Zs: source (or airgun) depth.
439 CTD: instrument for determining conductivity, temperature, depth and sound velocity.

Geophysics

440 Figure 5. Two dimensional forward modeling for sonobuoy 1103. a) Sonobuoy record
 441 section overlain with computed offset-time plot, RNMO-transformed to match reflection section
 442 in b). Sedimentary refractions extend farther to ~20 km offsets but here we only plot up to 16 km
 443 offsets for clarity. b) Stacked MCS reflection section overlain by velocity model. Selected
 444 refraction raypath (yellow) from layers 6 and 9 are shown. Reverberations of refractions P4 and
 445 P5 are marked as dashed lines in a). c) Same sonobuoy record low pass filtered (at 2-12Hz),
 446 linearly reduced to show deeper (crustal) refractions. Mult: multiple. d) Crustal model in depth
 447 domain, with all P-wave raypaths shown in thin white lines. Black bracketed numbers are S
 448 velocities, presided by Poisson's ratios. S12 and S13 in c) are converted S phases refracted from
 449 layers 12 and 13, with a modeled Poisson's ratio of .25, converted from P-wave at horizon 8
 450 (dashed red). Modified after Chian and Lebedeva-Ivanova, 2015 except S wave modeling.

451 Figure 6. Modeling of sonobuoy 1104. a) Sonobuoy record section NMO reduced at
 452 1.6km/s to match coincident reflection profile in b). Green lines show raypaths for converted S-
 453 refraction S7 for layer 7. The bracketed Poisson's ratio of 0.36 in layer 6 is assumed as S6 cannot
 454 be not modeled due to interferences. c) Same sonobuoy section NMO reduced to 4 km/s to show
 455 deeper crustal refractions at farther offsets. d) Coincident reflection profile at the same scale as
 456 c), overlain with all P-wave raypaths generating computed XT curves in c). Panels a)-d)
 457 modified after Chian and Lebedeva-Ivanova, 2015 except S wave modeling.

458 Figure 7. Fig. 7. Cartoon showing dominant P-S conversion interfaces for converted S
 459 waves in a marine sonobuoy setting. Solid raypath shows P-waves, while dashed raypath shows
 460 S-waves. Condition for “P-S conv 1” follows Eccles et al., 2009. Condition for “P-S Conv 2”
 461 applies to deeper crustal layers whose S-velocity (V_s) is greater than 4.2 km/s (i.e. V_t ; Fig. 9).

Geophysics

462 S-waves converted at any shallower horizons, if existing, will arrive later and therefore can be
463 obscured and not determinable, unless when their conversions are stronger than basement (e.g.
464 Figure 5).

465 Figure 8. Modeling sonobuoy 921-2. Raypath in d) shows S-refractions converted at the
466 top of layer 10 (S12) and from top of layer 11 (S13), and for M6 (double refraction of P6
467 bounced at the seafloor). Modified after Chian and Lebedeva-Ivanova, 2015 except S wave
468 modeling.

469 Figure 9. Modeling of sonobuoy 912. a) Sonobuoy record section RNMO reduced at
470 1.7km/s to match coincident reflection profile in b). c) Same sonobuoy section RNMO reduced
471 to 4 km/s to show deeper crustal refractions at farther offsets. d) Coincident reflection profile in
472 the depth domain, overlain with all S-wave raypaths. Modified after Chian and Lebedeva-
473 Ivanova, 2015 except S wave modeling.

474 Figure 10. a) Amplitude modeling of sonobuoy 912 at the same scale as Fig. 9c; inset
475 shows a comparison of computed amplitudes of P10 and S10 arrivals at two arrow locations.
476 Ratio of peak amplitudes of S10 and P10 as in the inset is measured to be 55%. b) Same
477 sonobuoy record section as Fig. 9c for comparison.

478 Figure 11. Re-modeling of sonobuoy record 1110 atop Alpha Ridge. a) Area fill display
479 of part of record section, overlain with traveltime curves from model in b) which was published
480 by Evangelatos et al. (2017). c) Same sonobuoy data displayed with 3D shading, overlain with
481 travelttime curves from new model in d). It can be seen that all recorded wide-angle reflections
482 and refractions can be modeled visually in detail and more layers can be modeled with the new

Geophysics

483 method presented in this paper. The previously conventional method, however, mostly ignored
484 the wide-angle energy of sonobuoy data during modeling.

485 Figure 12. Re-modeling of sonobuoy record 1110 for sub-basement structure. a)
486 Published crustal model of Evangelatos et al. (2017). b) Computed travel-time curves from this
487 published model. c) Revised crustal model based on the same data, with trace length extended
488 for modeling S phases in d). Selected raypaths shown in c) represent the S-phases from layers
489 10-12. e) The S phases are more emphasized in e) by using a smaller reducing velocity in
490 display. Note that the refraction P13 from the bottom layer is best modeled by a velocity of 7.2
491 km/s instead of the slower value of 6.9 km/s by Evangelatos et al. (2017), a change more
492 compatible with other nearby sonobuoys such as 1103 (Figure 5) and 1104 (Figure 6).

493

494

LIST OF TABLES

495 Table 1. Error analysis of layer velocities and depths for sonobuoy 1104 (Figure 6). dV/V
496 and dZ/Z are maximum deviation in percentage from average velocity and depth for each layer.
497 V1-V2 are range of average velocity for the two perturbed models. Ztop and Ttop are depth and
498 time of top horizon of each layer for the un-perturbed model. Bold lines indicate basement layer,
499 below which the error analysis method does not apply due to lack of control from reflection
500 profile.